aerospace

MDPI

Article

Multidisciplinary Optimization Design of an Airship Considering Temperature-Rise Effect

Wei Wang [1,2,*] and Jianliang Ai [1]

[1] College of Intelligent Robotics and Advanced Manufacturing, Fudan University, Shanghai 200433, China
[2] General Configuration Aerodynamic Institute, AVIC The First Aircraft Institute, Xi'an 710089, China
* Correspondence: wangw137@avic.com

Abstract

During stratospheric airship station-keeping missions, the pronounced temperature-rise effect directly affects aerodynamic drag and power generation efficiency, yet most existing design optimization studies tend to neglect it, potentially leading to biased performance assessments. Thus, an aerodynamic–thermal multidisciplinary optimization framework was developed in this study for a stratospheric airship considering temperature-rise effects. High-fidelity simulations were employed to construct surrogate models for drag coefficient and daily power generation, and these models were subsequently integrated into a multidisciplinary optimization framework aimed at minimizing the total system mass. The optimization results show that, compared with the baseline optimal design, the globally optimized configuration is slenderer, the location of the maximum diameter shifts forward, and the nose and tail contraction becomes smoother. For the solar array layout, the optimized design is also shifted forward, with a shorter axial coverage range, and greater concentration in the fore and middle regions of the envelope. The optimized configuration reduces the combined mass of the propulsion, energy, and structural subsystems, resulting in an approximately 10% reduction in the total system mass. These results demonstrate that incorporating temperature-rise effects into multidisciplinary optimization can significantly affect the optimal design and provide a more realistic assessment of stratospheric airship performance during station-keeping operations. Both Bas and Opt use the temperature-coupled surrogate models; therefore, their comparison evaluates the benefit of full-variable co-design rather than a temperature-on/temperature-off ablation.

Keywords: stratospheric airship; temperature-rise effect; multidisciplinary optimization design; surrogate model

Check for updates

Academic Editor: Kung-Ming Chung

Received: 16 July 2026
Revised: 24 August 2026
Accepted: 25 August 2026
Published: 31 August 2026

Copyright: © 2026 by the authors. Licensee MDPI, Basel, Switzerland. This article is an open access article distributed under the terms and conditions of the Creative Commons Attribution (CC BY) license.

1. Introduction

Stratospheric airships are typical long-endurance flight platforms. They use buoyancy to support their weight and to maintain sustained flight [1–3], while they achieve long-term station-keeping based on aerodynamic or aerostatic principles. They therefore play an important role in modern aerospace systems [4–6]. Typically, airships are equipped with solar cells and can remain aloft at high altitudes for long periods to perform early-warning and reconnaissance missions. They can also maintain a nearly fixed position relative to the ground for years, in a way that is similar to geostationary satellites. Because of their ultra-long endurance and stable payload environment, airships have attracted considerable attention in both academia and engineering. They are important not only for early warning,

surveillance, and reconnaissance, but also for emergency communication relay, disaster monitoring, high-altitude scientific exploration, and logistics transport [7,8].

Existing airship design methods usually assume a fixed envelope shape [9,10]. Under this design mode, aerodynamic drag reduction of the envelope plays a key role in lowering the overall energy consumption. A decrease in aerodynamic drag directly reduces the power required by the propulsion system for station-keeping, which then lowers the demand for solar arrays and energy storage batteries from the power requirement side. However, this single-disciplinary design logic based mainly on aerodynamic drag reduction has clear limits in the real thermal environment of the stratosphere. At stratospheric altitudes, the thin atmosphere leads to weak convective heat dissipation, while the solar radiation intensity is much higher than that near the ground. Modern airships commonly use large-area solar arrays as the main power source. However, photovoltaic systems have limited conversion efficiency. Even for the most efficient multi-junction solar cells, 65–70% of the incident solar radiation is still converted into waste heat rather than electricity [11]. This waste heat acts directly on the envelope surface and forms a strong local heat source. Moreover, the large surface area characteristic of stratospheric airships provides substantial exposure to solar radiation, making thermal effects a critical consideration in aerodynamic design. These additional thermal loads not only cause a significant reduction in the photovoltaic conversion efficiency of solar cells due to temperature-rise but also induce earlier boundary-layer separation near the aft part of the envelope. This may alter the boundary-layer development and consequently affect the aerodynamic drag characteristics of the envelope [12].

Therefore, airship design should not only consider the streamlined shape of the envelope, but also evaluate the photovoltaic system, propulsion system, and payload demand in an integrated way, so that the best overall performance can be achieved when temperature-rise effects are considered [13–15]. For example, the area of the solar array must be accurately matched with the power demand of the airship. An undersized array can cause power shortage, while an oversized array increases structural weight, potentially leads to irreversible structural changes [16], and reduces the payload capacity. Also, a higher temperature decreases the conversion efficiency of solar cells, so the system requires a larger solar array area to compensate for the power loss. But this adjustment also increases the envelope surface area and total weight, which then causes a secondary increase in aerodynamic drag and energy consumption. This complex trade-off among temperature variation, energy use, and drag control makes aerodynamic–thermal multidisciplinary design optimization (MDO) considering temperature-rise effects necessary [17].

In this study, the temperature-rise effect of an airship operating in the stratospheric environment was incorporated into an MDO framework. Existing studies still lack an optimization framework that includes both the thermal environment and drag requirement. Nine design variables related to the envelope shape and solar array layout were considered. The thermal, aerodynamic, geometric, and energy models were integrated into a unified optimization framework. Under the constraint of meeting the energy demand over the mission period, the optimization aimed to minimize the total system mass of the airship. The Bas and Opt cases both retain temperature coupling, so the reported comparison does not isolate the temperature-rise contribution.

2. Analysis Models

In this section, the disciplinary models used for optimization were divided into four main models outlined below.

The environment model describes the environmental parameters related to a specific station-keeping location. The geometry model defines the method used to generate the

envelope profile. The aerodynamic model describes the interaction between the above two models. In this model, the effect of the thermal environment on aerodynamic drag is considered, and a surrogate model is built for fast evaluation. The energy model describes the estimation process for the total supplied energy and the total required energy. In this part, the energy requirement is also evaluated efficiently through a surrogate model.

2.1. Environment Model

Stratospheric airships are usually designed to operate at a specific location and altitude, and their performance is highly sensitive to environmental conditions. The environment model provides the atmospheric parameters and solar radiation conditions required for thermal, aerodynamic, and energy analyses, including air density, ambient temperature, wind speed, and solar irradiance.

The atmospheric parameters can be estimated using the international standard atmosphere model to describe their variation with altitude. The standard atmospheric temperature is then corrected based on the environmental characteristics of the actual deployment region. For the stratospheric wind field, the ambient wind speed directly affects the aerodynamic drag and propulsion power demand of the airship. Therefore, it should be analyzed using the high-altitude wind characteristics of the target region. In this study, Beijing was selected as the deployment location. Based on related research results [18], the variations in the meridional and zonal wind components at different altitudes above Beijing were analyzed, as shown in Figure 1.

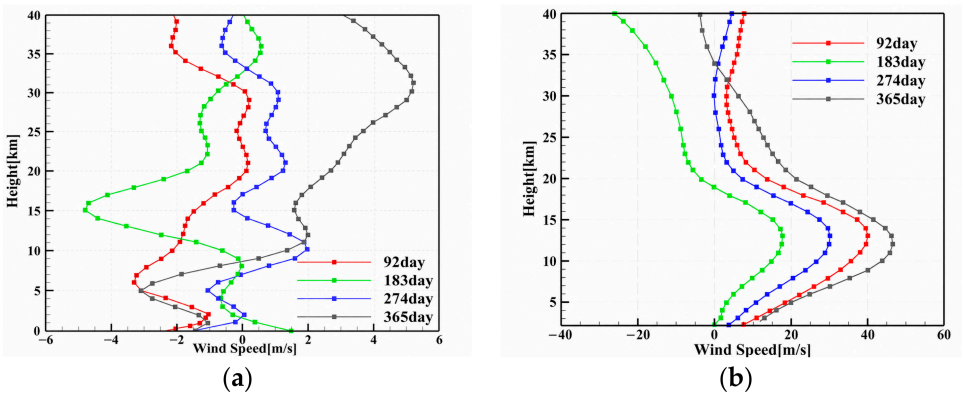


Figure 1. Variation of meridional and zonal wind components with altitude over Beijing: (**a**) meridional wind; (**b**) zonal wind.

As shown in Figure 1, within the stratospheric altitude range over Beijing, the zonal wind component is usually much larger than the meridional wind component. Therefore, the airship should be oriented along the east–west direction to reduce the headwind drag and lower the propulsion power demand. Also, near an altitude of about 20 km, a near-zero wind-speed region appears over Beijing in summer, which is favorable for airship station-keeping. Based on this analysis, typical deployment altitudes and design conditions were selected as the inputs of the environment model in the following design process, ensuring that the optimization results were grounded in a realistic engineering context.

2.2. Geometry Model

The Gertler Series 58 representation was used to generate the axisymmetric envelope profile from the maximum-diameter location m, nose radius r_o, tail radius r_1, and prismatic coefficient C_p. The detailed derivation and coefficient matrix are moved to Appendix A; only the final governing Equation (1) is retained in the main text.

The geometric definitions of these shape parameters are illustrated in Figure 2.

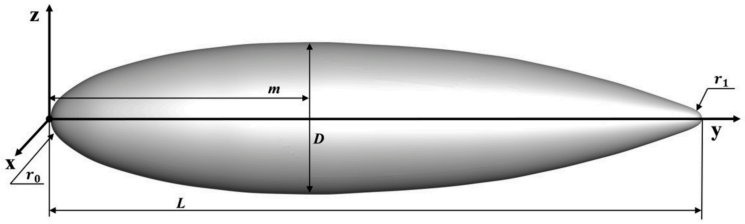


Figure 2. Schematic of airship envelope shape parameters.

After the coefficient system in Appendix A is solved, the envelope profile is given by

$$y(x) = D\sqrt{a_1\left(\frac{x}{L}\right) + a_2\left(\frac{x}{L}\right)^2 + a_3\left(\frac{x}{L}\right)^3 + a_4\left(\frac{x}{L}\right)^4 + a_5\left(\frac{x}{L}\right)^5 + a_6\left(\frac{x}{L}\right)^6} \quad (1)$$

where L is the envelope length, and D is the maximum envelope diameter. In this study, the fineness ratio is defined as $f = L/D$, and the envelope diameter is calculated from the envelope length and the fineness ratio.

Finally, based on this parametric model of the envelope shape, the solar array layout parameters can be further introduced. These parameters form the design variables used for surrogate-model construction and optimization and provide the basis for the following optimization problem.

2.3. Aerodynamic Model

The aerodynamic model considering temperature-rise effects is a key part of the multidisciplinary optimization of the airship. Its main task is to evaluate the drag characteristics of the airship based on the given shape parameters, environmental conditions, and surface thermal state, and to provide the basic data for the calculation of propulsion power demand. In traditional studies, many researchers [19,20] used the empirical formula proposed by Hoerner [21] to estimate the volumetric drag coefficient of the airship envelope. This type of method is simple and easy to use. However, the drag coefficient is mainly determined by the fineness ratio and Reynolds number, so it is not sensitive enough to detailed changes in the envelope profile. It also cannot reflect the effect of temperature rise on aerodynamic performance, so it cannot meet the needs of the envelope shape optimization in this study.

This study aimed to obtain the optimal envelope profile, so a high-accuracy method was needed to calculate the drag coefficient. If computational fluid dynamics (CFD) is directly coupled with the optimizer and high-fidelity analysis is performed for each candidate profile, the computational cost will be very high [22–24]. Therefore, a surrogate model of the drag coefficient considering temperature-rise effects was constructed in this study to achieve fast drag prediction.

2.3.1. Numerical Method

The aerodynamic samples were evaluated using the Reynolds-averaged mass, momentum, and energy conservation equations for low-Mach external flow. The airship surface was treated as a no-slip wall, and the instantaneous nonuniform temperature T_s obtained from the transient thermal model prescribed as the wall thermal boundary. Freestream pressure, temperature, density, and station-keeping wind speed were imposed at the outer boundary, with ambient pressure specified downstream.

A full circumferential domain was retained for nonuniform solar heating. Geometry-dependent body-fitted meshes use near-wall layers and local refinement around the nose, maximum-diameter region, afterbody, and wake. The same meshing logic was applied throughout the design space. The archived database retains the converged integral re-

sponses, but not every native mesh and solver log; therefore, unverified case-specific cell counts and grid histories were not introduced in this revision.

2.3.2. Construction of the Aerodynamic Surrogate Model

1. Design variables

In this study, nine independent design variables were selected. They include the key parameters of the airship envelope shape and the layout parameters of the solar array and are used to describe the main design factors that affect the drag and energy characteristics of the airship as fully as possible. The physical meaning, range, and constraints of each design variable are listed in Table 1.

Table 1. Design variables and ranges.

Design Variable	Description	Range	Constraint
m	Location of maximum diameter	0.3–0.6	
r_0	Nose radius of curvature	0–1	
r_1	Tail radius of curvature	0.1–1	
C_p	Prismatic coefficient	0.55–0.7	$0 < Y_f < L$
f	Fineness ratio	2.5–5	$0 < Y_s < L$
L, (m)	Envelope length	100–300	$Y_f - Y_s > 1$ m
Y_s, (m)	Starting position of solar array	20–100	
Y_f, (m)	Ending position of solar array	50–200	
ψ, (deg)	Wrap angle of solar array	50–180	

2. Surrogate model training and accuracy validation

To ensure that the training samples are sufficiently uniform and representative in the design space, the Latin hypercube sampling (LHS) method [25] was used to generate the training sample set. Considering the dimension of the design variables, model complexity, and cost of high-fidelity analysis, 180 training samples were generated in this study. The drag coefficient of each sample was then calculated using the high-fidelity analysis model, forming the input-output dataset required for surrogate model training.

Another 10 independent LHS samples were used for validation. RSM [26], Kriging [27], and RBF [28] were compared using MARE, MAXRE, and RRMSE, which are relative errors normalized by the corresponding high-fidelity value and reported in percent.

The prediction accuracy of the three aerodynamic surrogate models is summarized in Table 2.

Table 2. Prediction accuracy of different surrogate models for drag coefficient.

Surrogate Model Type	Accuracy Metric	Relative Error in C_d (%)
RSM	MARE	4.03
	MAXRE	6.69
	RRMSE	4.56
Kriging	MARE	0.69
	MAXRE	1.48
	RRMSE	0.78
RBF	MARE	1.32
	MAXRE	1.63
	RRMSE	1.31

The evaluation results show that the Kriging model achieves high global average prediction accuracy and also performs better than the other two models in controlling local extreme errors. This indicates that the Kriging model has strong prediction ability over the

whole design space. Figure 3 shows the scatter comparison between the CFD simulation values and the predicted values of the Kriging model for the 10 validation samples.

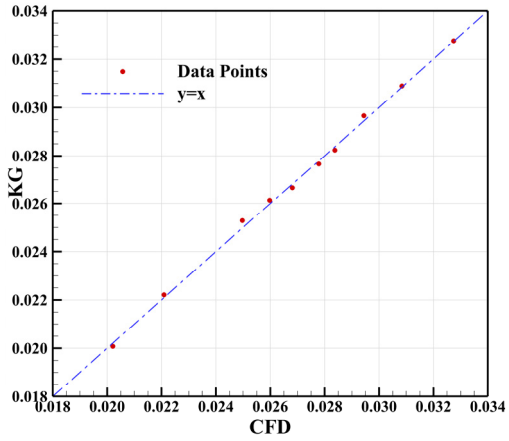


Figure 3. High-fidelity versus Kriging-predicted drag coefficients for the validation samples.

All validation points lie close to the 1:1 line, confirming the accuracy of the Kriging surrogate for the retained high-fidelity samples.

As external supporting benchmarks, Zhang and Wang [29] reported a 1.5% mean drag error for an airship-hull CFD procedure validated against six streamlined-body experiments, while Lv et al. [30] validated a solar array airship thermal formulation against a ground experiment. These studies support the adopted physical modeling route; the 10 independent samples above remain the direct validation of the present surrogates.

2.3.3. Drag Coefficient Correction

The total drag includes the envelope and appendages. Hoerner [21] and later airship studies [31] support a complete-vehicle correction. In this conceptual model, k = 1.8 is used as a consistent engineering allowance for unmodeled appendages, rather than as a universal value taken directly from Ref. [31].

2.4. Transient Thermal Model

The surface temperature is advanced transiently as the solar position changes. At each time step, the local energy balance includes direct and diffuse solar radiation, external convection, long-wave infrared radiation, conduction through the envelope/solar array layers, and the electrical energy extracted by photovoltaic conversion.

The environmental model supplies the ambient state, wind speed, solar irradiance, and solar direction. A UDF updates the surface heat flux and temperature field. The resulting nonuniform T_s field is used as the aerodynamic wall-temperature boundary and is integrated over the photovoltaic area and daylight period to obtain daily generated electrical energy.

2.5. Energy Model

The energy model is used to evaluate the energy generation and consumption of the airship under a day–night cycle. It is one of the core models for determining whether the airship can maintain continuous station-keeping flight. This model mainly includes three parts: daily power generation of the solar array, propulsion power consumption, and energy storage demand analysis. The daily power generation is predicted efficiently by a surrogate model.

2.5.1. Daily Power Generation and Surrogate Model Construction

The heat-source terms on the surface elements of the solar array are shown in Figure 4. The energy used for power generation is defined in the UDF program as part of the heat loss of each surface element and is directly obtained from the high-fidelity calculation.

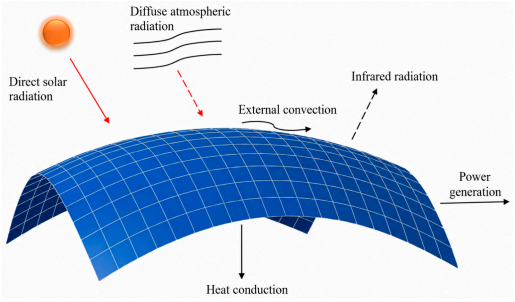


Figure 4. Schematic of heat-source terms on solar array surface elements.

Similar to the construction of the aerodynamic surrogate model, nine independent design variables were selected in this study. The physical meaning, range, and constraints of each design variable are listed in Table 3. The LHS method was used to generate 180 training samples. The daily power generation of each sample was obtained through high-fidelity calculation, forming the input–output dataset required for surrogate model training.

Table 3. Prediction accuracy of different surrogate models for daily generated electrical energy.

Surrogate Model Type	Accuracy Metric	Relative Error in E_{gen} (%)
RSM	MARE	3.61
	MAXRE	5.71
	RRMSE	3.85
Kriging	MARE	0.55
	MAXRE	1.23
	RRMSE	0.62
RBF	MARE	1.20
	MAXRE	1.52
	RRMSE	1.24

Another 10 independent LHS samples were used to validate the RSM, Kriging, and RBF energy surrogates. The MARE, MAXRE, and RRMSE values in Table 3 are relative percentage errors normalized by the high-fidelity daily generated energy.

Figure 5 compares the high-fidelity daily generated electrical energy with the Kriging predictions for the 10 validation samples.

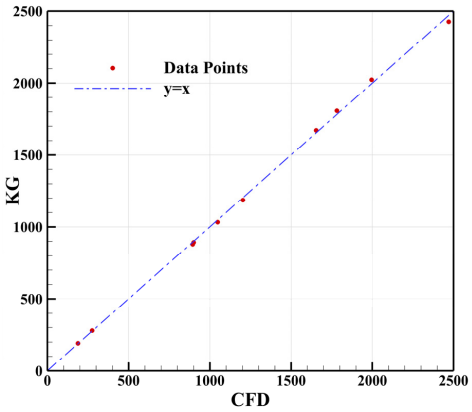


Figure 5. High-fidelity versus Kriging-predicted daily generated electrical energy for the validation samples.

It can be seen that the Kriging model gives the best prediction accuracy and the strongest generalization capability among the three surrogate models. It can therefore replace high-fidelity CFD simulation with good accuracy and enables fast prediction of the daily power generation of the airship.

2.5.2. Propulsion Power Consumption and Energy Storage Demand Analysis

The thrust-system power P_{thrt} required to balance the total drag D_{tot} at station-keeping wind speed V is calculated as follows:

$$P_{\text{thrt}} = \frac{D_{\text{tot}} v}{\eta_{\text{P}} \eta_{\text{g}}} \tag{2}$$

where D_{tot} is total drag, v is ambient wind speed, and η_P and η_g are the propulsive and gear efficiencies, respectively.

The total power demand P_{tot} is the sum of thrust-system power P_{thrt}, payload power P_{pay}, and control-system power P_{cont}:

$$P_{\text{tot}} = P_{\text{thrt}} + P_{\text{pay}} + P_{\text{cont}} \tag{3}$$

In this study, the control system power was set to 10% of the payload power.

The required daily energy E_{req} includes the daytime demand and the stored nighttime demand, including storage-conversion losses:

$$E_{\text{req}} = P_{\text{tot}} t_{\text{day}} + \frac{P_{\text{tot}} t_{\text{night}}}{\eta_{\text{conv}}} \tag{4}$$

where t_{day} and t_{night} are the daytime and nighttime durations, respectively, and η_{conv} is the energy storage conversion efficiency.

The day–night energy constraint is $E_{\text{gen}} - E_{\text{req}} \geq 0$, where E_{gen} is the daily generated electrical energy and E_{req} is the required daily energy.

3. Mass Estimation

The system mass model was used to evaluate the total mass of the airship. Together with the buoyant lift provided by the envelope, it determines whether a design satisfies the buoyancy-weight balance requirement. The buoyancy is calculated as follows:

$$B = \rho_a V_{env} g \tag{5}$$

where B is buoyant force, ρ_a is ambient-air density, V_{env} is envelope volume, and g is gravitational acceleration.

The total mass of the airship is usually composed of the envelope structural mass, energy system mass, propulsion system mass, payload mass, and other auxiliary system masses.

The total mass of the structural subsystem is calculated as follows:

$$m_{strt} = m_{gas} + m_{env} + m_{fin} + m_{misc} \tag{6}$$

where m_{gas}, m_{env}, m_{fin}, and m_{misc} are the gas, envelope, fin, and miscellaneous masses, respectively.

$$m_{He} = \rho_a V_{env} \frac{\mathrm{M}_{He}}{\mathrm{M}_{air}} \tag{7}$$

https://doi.org/10.3390/aerospace13090794

where M_{He} and M_{air} are the molar masses of helium and air, respectively.

$$m_{env} = 1.2\rho_{fab}A_{env} \tag{8}$$

where ρ_{fab} is the envelope-material areal density, and A_{env} is the envelope surface area; the factor 1.2 accounts for reinforcements and installation items:

$$m_{fin} = 1.2\rho_{fab}A_{fin} \tag{9}$$

Here, the coefficient 1.2 is also used to account for the additional weight caused by the fin support structure and internal structure.

The surface area of the fins is estimated using the empirical formula proposed by Colozza and Dolce [16], viz.,

$$A_{fin} = 0.0121V_{env} \tag{10}$$

Colozza and Dolce derived $A_{fin}/V_{env} = 0.0121\ \mathrm{m}^{-1}$ from existing airships but did not report a formal fineness-ratio calibration interval. Their representative high-altitude design used f = 4.0; the present optimum f = 4.259 is close to this value. The relation is therefore retained for conceptual estimation, with detailed stability and tail-load verification reserved for later design stages.

The mass of other miscellaneous components of the stratospheric airship is taken as 25% of the total mass of the envelope, fins, energy subsystem, and propulsion subsystem:

$$m_{misc} = 0.25(m_{env} + m_{fin} + m_{ener} + m_{thrt}) \tag{11}$$

The mass of the energy system is the sum of the solar array mass and the energy storage system mass:

$$m_{ener} = m_{pv} + m_{stor} \tag{12}$$

The mass of the propulsion system is calculated as follows:

$$m_{thrt} = P_{thrt}/w_{thrt} \tag{13}$$

where w_{thrt} is the thrust-system specific power.

The total mass of the airship is given by

$$m_{tot} = m_{thrt} + m_{strt} + m_{ener} + m_{pay} \tag{14}$$

During the optimization process, the system mass is used not only to construct the objective function but also to compare with the effective buoyant lift of the airship, so that whether a given design satisfies the buoyancy-weight balance constraint can be determined. Therefore, the system mass model is an important link between shape design, energy-system design, and overall feasibility analysis.

4. Optimization Problem Formulation

4.1. Optimization Framework

With the payload, station-keeping altitude, endurance time, and basic flight conditions specified, the study now focused on improving the overall performance of the airship by adjusting the envelope shape and solar array layout parameters. To fully consider the effect of temperature rise on the aerodynamic characteristics and optimization results, the multidisciplinary optimization framework shown in Figure 6 was established.

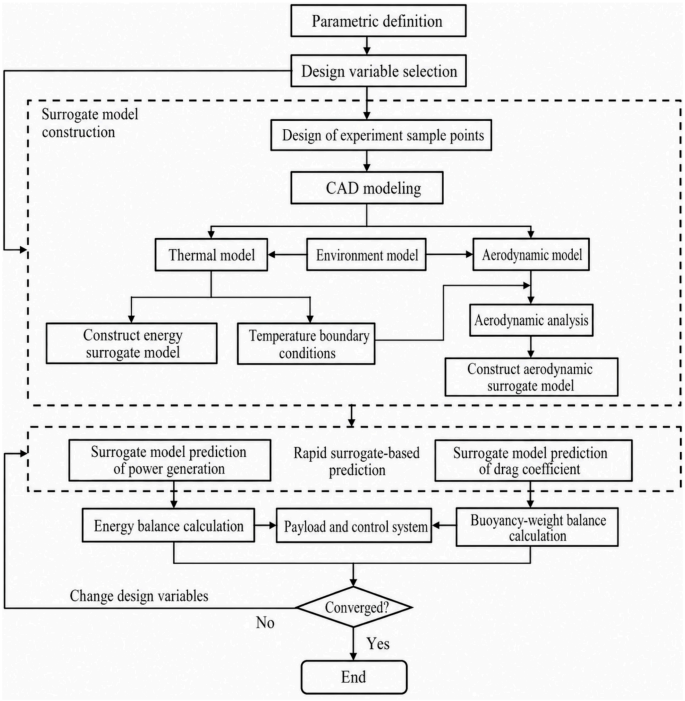


Figure 6. Multidisciplinary optimization design framework for the airship.

4.2. Design Variables and Baseline Configuration

4.2.1. Design Variables

As described above, the design variables in this study include the envelope geometric parameters and the solar array layout parameters, as shown in Figure 7.

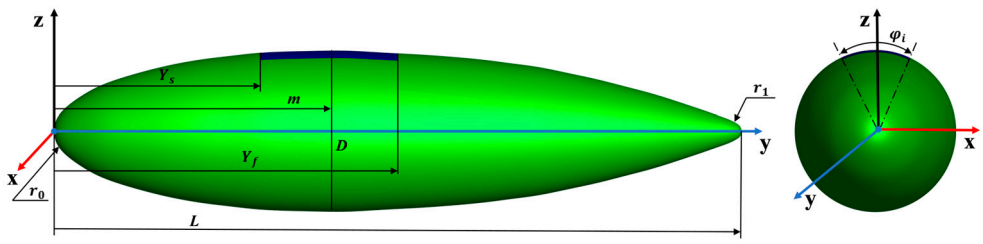


Figure 7. Schematic of design variables.

Six parameters are used to control the geometric deformation of the envelope, including the location of the maximum diameter, nose radius, tail radius, prismatic coefficient, fineness ratio, and envelope length. These parameters define the envelope profile and overall size. Three parameters are used to control the solar array layout, including the starting position, ending position, and wrap angle of the solar array. They determine the mounting position and circumferential coverage of the solar array on the envelope. The design variables and their ranges are listed in Table 4.

Table 4. Design variables and value ranges.

Design Variable	Range	Unit
m	0.3–0.6	—
r_0	0–1	—
r_1	0.1–1	—
C_p	0.55–0.7	—
f	2.5–5	—
L	100–300	m

Table 4. *Cont.*

Design Variable	Range	Unit
Y_s	20–100	m
Y_f	50–200	m
ψ	50–180	deg

At the same time, some parameters are kept constant during the optimization process. These parameters are treated as design constants and do not directly participate in the optimization. Table 5 lists the design constants used in this study. Their values were determined based on the assumed requirements of the user organization and the current level of technology.

Table 5. Design constants and values.

Design Constant	Description	Value
m_{pay}	Payload mass	500 kg
P_{pay}	Payload power	3 kW
P_{cont}	Control system power	0.3 kW
η_{thrt}	Propulsive efficiency	90%
η_{pv}	Solar array efficiency	12%

4.2.2. Baseline Configuration

The geometric design of the envelope is a key part of airship design. In recent years, several studies investigated optimal aerodynamic shapes for airships under different application scenarios. As a result, several standard profiles were proposed, such as GNVR, ZHIYUAN-1, and WANG. The envelope curves of these standard profiles are shown in Figure 8.

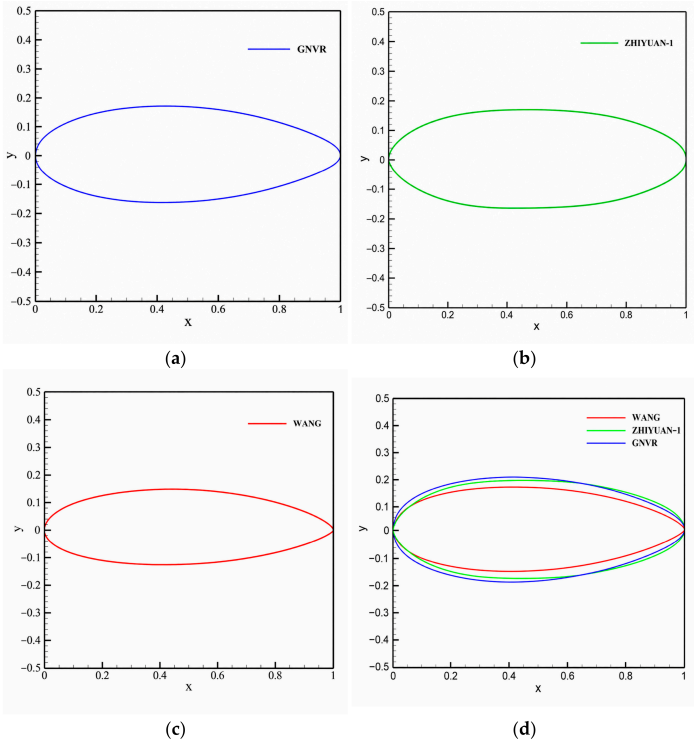


Figure 8. Comparison of standard envelope profiles: (**a**) GNVR; (**b**) ZHIYUAN-1; (**c**) WANG; (**d**) combined comparison.

Table 6 lists the design-variable values of the above standard profiles. In this study, the GNVR profile was selected as the baseline configuration for comparison. To verify the importance of shape optimization, the first five design variables of the GNVR profile are fixed during the optimization, while the envelope length and solar array layout parameters are allowed to vary.

Table 6. Design-variable parameters of standard profiles.

Standard Profile	m	r_0	r_1	C_p	f
GNVR	0.415	0.600	0.180	0.615	3.044
ZHIYUAN-1	0.419	0.377	0.251	0.651	3.266
WANG	0.404	0.600	0.100	0.610	3.859

4.3. Objective Function and Constraints

The objective of this study was to obtain the optimum value of the objective function. The objective function to be minimized is the total system mass of the airship, which is calculated using Equation (15):

A single total-mass objective is appropriate because payload, altitude, location, and endurance are fixed, while drag, propulsion power, photovoltaic area, storage demand, and structural size all propagate into subsystem mass. Buoyancy and day–night energy balance are imposed as feasibility constraints. A multi-objective formulation would be more appropriate when mission-level quantities such as payload, endurance, cost, or robustness are also treated as competing objectives [32]:

$$\min : m_{tot} \Rightarrow m_{tot} = m_{thrt} + m_{strt} + m_{ener} + m_{pay} \tag{15}$$

During station-keeping, the constraints are $0 < Y_f < L$, $0 < Y_s < L$, $Y_f - Y_s > 1$ m, $B - m_{tot}g \geq 0$, $E_{gen} - E_{req} \geq 0$.

$$\begin{gathered} 0 < Y_f < L \\ 0 < Y_s < L \\ Y_f - Y_s > 1 \text{ m} \\ B - m_{tot}g \geq 0, \quad I_{day} = I_{design} \\ E_{gen} - E_{req} \geq 0, \quad I_{day} = I_{design} \end{gathered} \tag{16}$$

The optimization problem is defined in Table 7.

Table 7. Definition of the optimization problem.

	Variable	Lower Bound	Upper Bound	Unit
Optimization Objective	m_{tot}	—	—	—
Design Variable	m	0.3	0.6	—
	r_0	0	1	—
	r_1	0.1	1	—
	C_p	0.55	0.7	—
	f	2.5	5	—
	L	100	300	m
	Y_s	20	100	m
	Y_f	50	200	m
	ψ	50	180	deg
Constraint	Y_s	0	L	m
	Y_f	0	L	m
	$Y_f - Y_s$	1	—	m
	$m_{tot}g$	0	B	N
	E_{req}	0	E_{gen}	kWh

Finally, the mathematical formulation of the optimization problem can be written as Equation (17):

$$\begin{aligned} &\min \quad m_{tot} \\ &w.r.t \quad x \in R^n \\ &\text{s.t.} \quad 0 < Y_s < L \\ &\qquad 0 < Y_{\mathrm{f}} < L \\ &\qquad Y_{\mathrm{f}} - Y_{\mathrm{s}} > 1\ \mathrm{m} \\ &\qquad B - m_{tot} g \geq 0, \quad I_{day} = I_{design} \\ &\qquad E_{gen} - E_{req} \geq 0, \quad I_{day} = I_{design} \\ &x = \left[m, r_0, r_1, C_p, f, L, Y_s, Y_f, \psi \right]^{\mathrm{T}} \end{aligned} \tag{17}$$

4.4. Optimization Algorithm

To solve the multidisciplinary optimization problem of the airship established in this study, the genetic algorithm (GA) [33,34] was selected as the optimization method.

The real-coded GA uses a population of 100, a maximum of 200 generations, crossover probability 0.80, mutation probability 0.10, and five elite individuals. The run stops at 200 generations or when the relative change in the best feasible mass is below 10^{-6} for 30 consecutive generations.

GA is a stochastic optimization method with strong robustness and global search capability. Unlike gradient-based optimization methods, GA performs a population-based parallel search. It can examine multiple candidate solutions in the design space at the same time, reducing the possibility of being trapped in a local optimum and improving the chance of finding the global optimum, as shown in Figure 9. This method calculates the fitness of each individual using the objective function and then updates the population through genetic operations such as selection, crossover, and mutation. It has low requirements on the analytical properties of the objective function and usually does not require the function to be continuous or differentiable. Therefore, GA is suitable for engineering optimization problems with many variables, strong nonlinearity, and a complex solution process.

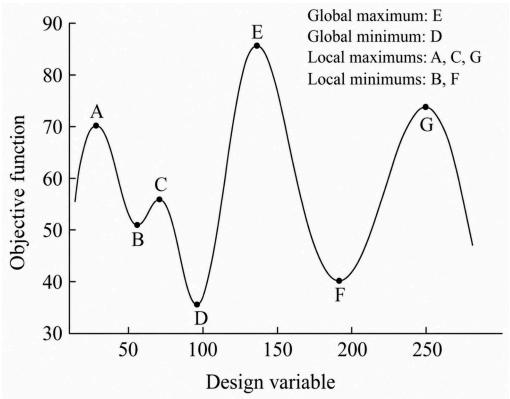


Figure 9. Schematic illustration of global and local optima [35].

The multidisciplinary optimization design of an airship involves several disciplines, including aerodynamics, thermal analysis, energy, and environment. These disciplines are strongly coupled, and the design problem has a high-dimensional design space with a wide range of variables. GA can adapt well to this type of complex optimization problem. Related studies have also applied GA to the multidisciplinary optimization design of high-altitude airships [32,36] and obtained good results, which indicates that GA is suitable for solving the multidisciplinary optimization problem of airships.

5. Results and Discussion

5.1. Comparison Between the Baseline Optimal Design and the Global Optimal Design

All the optimization results in this study were obtained for a stratospheric airship deployed at a specific geographical location, namely Beijing. The configuration optimized based on the GNVR profile is denoted as "Bas", and the final optimized configuration is denoted as "Opt". Thus, Bas–Opt isolates the benefit of expanding the design space within the coupled framework, not the isolated thermal effect.

Figure 10 compares the envelope geometries of the baseline optimal design (Bas) and the global optimal design (Opt). The geometric differences between the two configurations are mainly reflected in three aspects: the overall scale ratio, the location of the maximum cross-section, and the contraction pattern of the nose and tail.

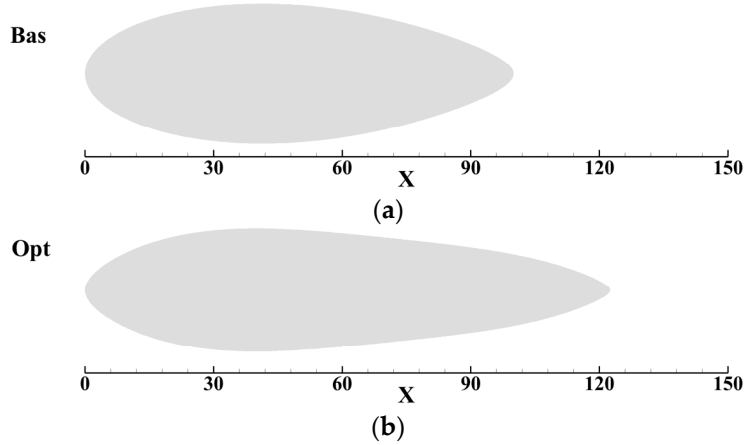


Figure 10. Geometric comparison between the Bas and Opt configurations: (**a**) Bas; (**b**) Opt.

- Compared with the Bas configuration, the envelope of the Opt configuration is clearly elongated in the axial direction, while its transverse bulge is reduced. The fineness ratio is much higher, and the overall shape becomes slenderer and more streamlined.
- The maximum diameter of the Opt configuration is still located in the fore-middle part of the envelope, but the bulged region extends over a longer axial range. The transition from the forebody to the midbody becomes smoother. Compared with the Bas configuration, the connection among the forebody, midbody, and afterbody is more continuous.
- The nose of the Opt configuration is slightly sharper and longer, and the geometric variation near the nose becomes smoother. This indicates a more refined nose curvature distribution and a more streamlined nose shape. The tail is also clearly extended, and the afterbody contraction becomes smoother. The optimized configuration reduces the local curvature variation near the nose and tail and improves the continuity of the overall shape.

Overall, the optimization process does not simply enlarge or shrink a local region. Instead, it adjusts several geometric design variables in a coupled way, and these variables jointly determine the overall shape characteristics of the airship.

Table 8 compares the design variables of Bas and Opt. Compared with the baseline optimal design, the fineness ratio of the global optimal configuration increases from 3.044 to 4.259, and the length increases from 100 m to 122.6 m. The location of the maximum diameter decreases from 0.415 to 0.326, and the tail radius decreases from 0.180 to 0.101. These changes indicate that the optimized envelope becomes considerably slenderer, the maximum bulge moves forward, and the tail contraction becomes sharper and thinner. This is consistent with the previous parametric analysis, which shows that a larger fineness

ratio, a smaller tail radius, and a more forward maximum diameter location help reduce drag. In terms of drag reduction, the total drag coefficient of the airship decreases from 0.03634 to 0.03287, with a reduction of about 9.55%. This indicates that the optimized shape improves the aerodynamic performance and reduces the propulsion power demand, thereby reducing the system mass.

Table 8. Comparison of design variables between Bas and Opt.

Design Variable	Bas	Opt
m	0.415	0.326
r_0	0.600	0.529
r_1	0.180	0.101
C_p	0.615	0.592
f	3.044	4.259
L	100	122.6
Y_s	40	21.9
Y_f	87.5	68.5
ψ	180	180

Figure 11 shows the geometric characteristics of the solar arrays for the Bas and Opt configurations. It can be seen that the difference in the solar array layout is mainly reflected in the forward shift of the axial position and the reduction in the coverage length. In the Bas configuration, the solar array is placed relatively far downstream. Its starting position is near the middle of the envelope, and its ending position extends to the mid-aft region, so the axial coverage accounts for a large proportion of the envelope length. In the Opt configuration, the solar array moves clearly forward. Its starting position moves to the fore-middle region, and its ending position also moves forward. As a result, the overall coverage length is shortened, and the array is more concentrated on the fore-middle region of the upper envelope surface.

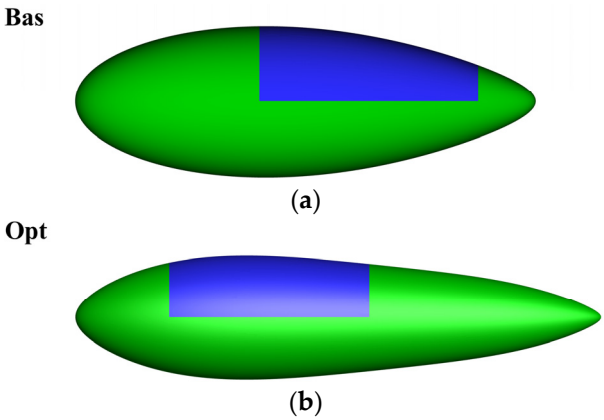


Figure 11. Geometric characteristics of solar arrays for the Bas and Opt configurations: (**a**) Bas; (**b**) Opt.

Consistent with Table 8, the optimization does not further increase the axial coverage of the solar array. Although placing the solar array mainly in the fore-middle region reduces its total coverage length, it helps reduce the mass of the solar energy system. Accordingly, the solar array surface area decreases from 2067 m^2 to 2024 m^2, corresponding to a reduction of about 2.08%.

Table 9 compares the key output parameters of the Bas and Opt configurations. From the overall output parameters, the envelope volume of the Opt configuration decreases from 51,966 m^3 to 47,160 m^3, corresponding to a reduction of about 9.25%. This indicates that the optimization reduces the required overall scale, which is beneficial for lowering

the mass of the envelope and the structural systems. Although the envelope surface area increases from 7991 m^2 to 8224 m^2 and the total power generation decreases from 684 kWh to 602 kWh, this result shows that the optimization does not take power generation capacity as the dominant objective. Instead, it accepts a certain decrease in power generation while satisfying the basic energy requirement, in exchange for a smaller volume, lower drag, and smaller solar array area.

Table 9. Comparison of key output parameters between Bas and Opt.

Output Parameter	Description	Bas	Opt
$V_{env}(m^3)$	Envelope volume	51,966	47,160
$A_{env}(m^2)$	Envelope surface area	7991	8224
$A_{pv}(m^2)$	Solar array surface area	2067	2024
C_{d_tot}	Total drag coefficient of the airship	0.03634	0.03287
E_{gen}(kWh)	Daily generated electrical energy	684	602

Figure 12 shows the subsystem mass comparison between the Bas and Opt configurations. It can be seen that the Opt configuration has lower propulsion system mass, energy system mass, and structural system mass than the Bas configuration, while the payload mass remains unchanged. Therefore, the reduction in total mass after optimization mainly comes from the combined decrease in these three parts, with the energy system and structural system making the largest contributions. This trend is consistent with the previous analysis. After optimization, the solar array coverage is shortened and the total power generation decreases, while the propulsion power demand is also reduced. These changes finally lead to a clear decrease in the mass of the energy system. The structural system mass decreases from 2350.13 kg to 2230.84 kg, with a reduction of about 5.08%. The energy system mass decreases from 1653.10 kg to 1307.27 kg, with a reduction of about 20.93%. This indicates that although the optimized envelope becomes longer and its surface area increases slightly, the structural mass is still reduced because the overall volume and system scale are decreased. The payload mass is fixed by the mission requirement and is not adjusted during optimization, so it remains 500 kg.

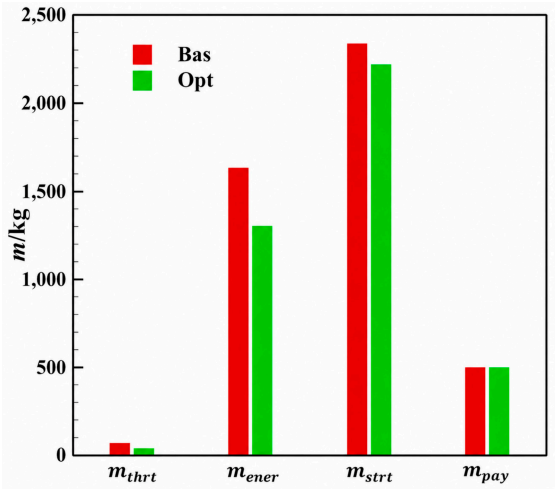


Figure 12. Subsystem mass comparison between the Bas and Opt configurations.

Overall, the Bas configuration has a larger volume and higher power generation, but this comes at the cost of higher drag and a larger system scale. The Opt configuration reduces drag, decreases volume, and reduces the solar array area by increasing the envelope fineness ratio and contracting the solar array layout. It is therefore more consistent with

the optimization objective of minimizing the total system mass of the airship. This shows that, for multidisciplinary optimization design of airships, the optimal design is not the one with the best single performance metric, but a comprehensive result that achieves a more reasonable balance among aerodynamics, energy, and mass.

The 9.55% reduction in C_d is larger than the Kriging maximum relative validation error (1.48%) and the RRMSE (0.78%). This comparison supports the aerodynamic trend; it is not a formal uncertainty bound on the propagated total-mass result.

Based on the reported bounds and Bas–Opt changes, fineness ratio f and maximum-diameter location m are the clearest aerodynamic design levers; the tail radius r_1 is also important because the optimum approaches its lower bound. The solar array variables affect drag mainly through the mapped temperature field and primarily control the energy-system performance. This interpretation is consistent with the published global-sensitivity trends in Ref. [29], although no new sensitivity indices are claimed here.

5.2. Effect of Date on Solar Array Performance

Because the incident solar radiation changes over the year, the power-generation capability of different regions of the same solar array also varies with season. Figure 13 shows the power-generation contours of the solar array on three representative dates, namely the winter solstice, summer solstice, and autumn equinox, and at three representative times, namely morning (1 h after sunrise), noon (12:00), and evening (1 h before sunset). It can be seen that the date changes the illuminated location and coverage on the solar array, which then affects the overall energy absorption of the array.

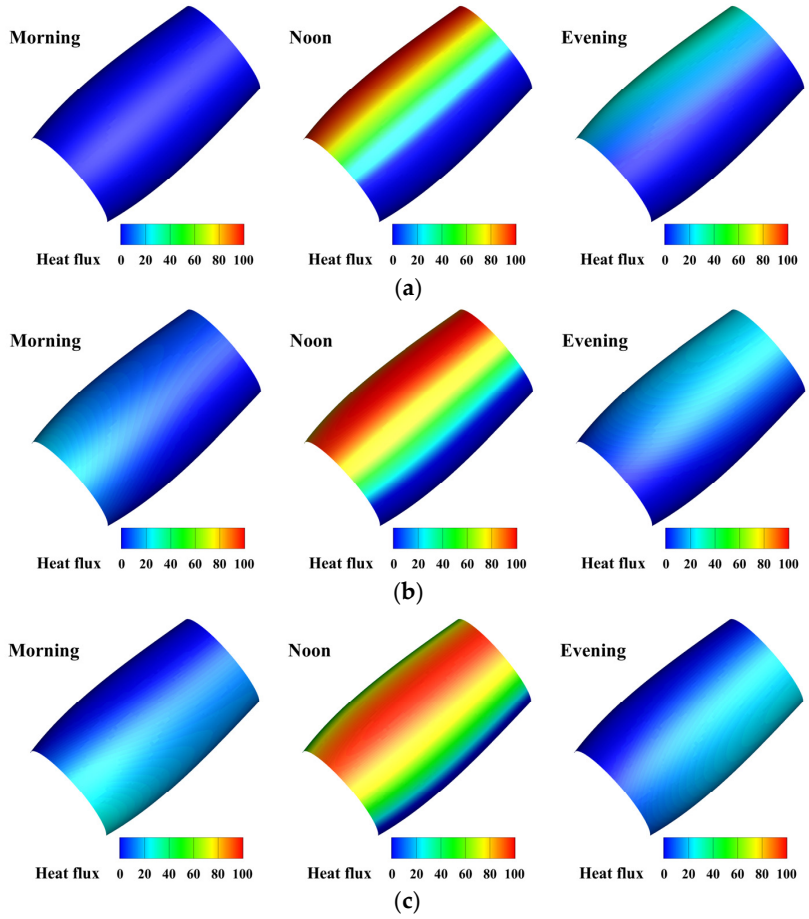


Figure 13. Power-generation contours of the solar array on representative dates and at representative times: (**a**) winter solstice; (**b**) autumn equinox; (**c**) summer solstice.

Figure 14 shows the power-generation curves of the solar array for the three representative dates and times. The power output first increases and then decreases with time, and the peak always appears at noon. Compared with the winter solstice, the peak power is clearly higher on the summer solstice and the autumn equinox. The highest value occurs on the summer solstice, with an increase of about 30%, while the autumn equinox is the second highest, with an increase of about 20%. In addition, as the season changes from the winter solstice to the summer solstice, the daylight duration gradually increases, from 8.5 h in winter to 11 h at the autumn equinox, and then to 14 h at the summer solstice. This change is directly reflected by the obvious widening of the power curve along the horizontal axis. The combined effect of higher peak power and longer sunshine duration makes the power-generation capability on the summer solstice much higher than that on the winter solstice. Therefore, the winter solstice is usually taken as the most unfavorable condition for the annual energy supply of the system.

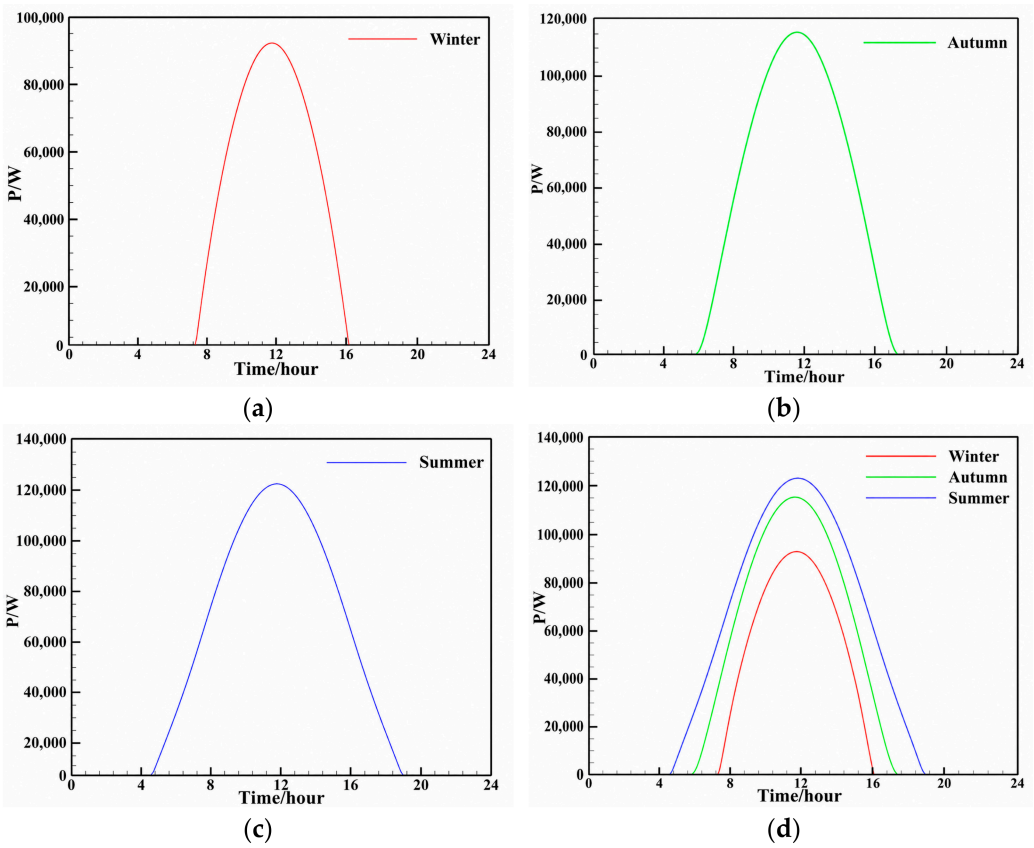


Figure 14. Power-generation curves of the solar array on representative dates and at representative times: (**a**) winter; (**b**) autumn; (**c**) summer; (**d**) comparison.

The above results show that the power-generation capability of each region of the solar array is strongly affected by both the season and time of day. Therefore, in addition to the geometric parameters of the envelope, it is necessary to include the geometric characteristics and layout variables of the solar array in the multidisciplinary optimization framework.

5.3. Scope of the Thermal Comparison

A matched temperature-on/temperature-off comparison would require a second temperature-independent high-fidelity database, independent surrogate validation, and a new nine-variable optimization. The present archive contains only the temperature-coupled dataset. Accordingly, the current results are interpreted as a coupled Bas–Opt design-space comparison; a matched thermal ablation is retained as future work.

6. Conclusions

This study focused on a stratospheric airship and investigated the aerodynamic–thermal multidisciplinary design problem under temperature-rise effects. A multidisciplinary optimization framework was established by coupling the environment model, geometry model, aerodynamic model, and energy model. The optimization design was then carried out with the objective of minimizing the total system mass. The main conclusions are as follows:

- To meet the needs of multidisciplinary optimization design of the airship, mapping relationships between the design variables and the drag coefficient and daily power generation were established using different surrogate modeling methods. By comparing the prediction accuracy of different models, the Kriging model was found to have the best overall accuracy and the strongest generalization capability.
- The mass reduction of the airship system mainly comes from the combined decrease in the propulsion, energy, and structural subsystems, with the energy and structural subsystems making more obvious contributions. The Opt configuration has lower propulsion system mass, energy system mass, and structural system mass than the Bas configuration. The structural system mass decreases from 2350.13 kg to 2230.84 kg, with a reduction of about 5.08%, while the energy system mass decreases from 1653.10 kg to 1307.27 kg, with a reduction of about 20.93%. This indicates that although the optimized envelope becomes longer and its surface area increases slightly, effective system-level mass reduction is still achieved because the overall volume decreases, the propulsion power demand is reduced, and the solar array area is smaller.
- The power-generation capability of the solar array changes clearly with season and time of day. Therefore, in addition to the geometric parameters of the envelope, the solar array layout parameters should also be considered in multidisciplinary optimization.

Author Contributions: Conceptualization, W.W. and J.A.; methodology, W.W.; software, W.W.; validation, W.W.; formal analysis, W.W.; investigation, W.W.; data curation, W.W.; writing—original draft preparation, W.W.; writing—review and editing, J.A.; visualization, W.W.; supervision, J.A.; project administration, J.A. All authors have read and agreed to the published version of the manuscript.

Funding: This research received no external funding.

Institutional Review Board Statement: Not applicable.

Informed Consent Statement: Not applicable.

Data Availability Statement: The datasets generated and analysed in this work are available from the corresponding author upon reasonable request.

Conflicts of Interest: The authors declare no conflict of interest.

Appendix A. Gertler Series 58 Polynomial Derivation

For completeness, the original derivation and Equations (A1)–(A22) are collected below without changing their numbering:

$$y^2 = a_1 x + a_2 x^2 + a_3 x^3 + \ldots + a_n x^n \tag{A1}$$

where $a_1, a_2, a_3, \ldots, a_n$ are determined by the shape parameters, including the location of the maximum diameter (m), the nose radius (r_o), the tail radius (r_1), and the prismatic coefficient (C_p), as shown in Figure 2.

To ensure that the generated shape satisfies the geometric constraints of the airship envelope, the polynomial coefficients are solved under the nose and tail boundary conditions,

derivative conditions, and curvature conditions. Specifically, when $x = 1$, $y = 0$; when $x = m$, $y = 1/2$ and $\frac{dy}{dx} = 0$. Thus, the following relations can be obtained:

$$a_1 + a_2 + a_3 + \ldots + a_n = 0 \tag{A2}$$

$$a_1 m + a_2 m^2 + a_3 m^3 + \ldots + a_n m^n = \frac{1}{4} \tag{A3}$$

$$a_1 + 2a_2 m + 3a_3 m^2 + \ldots + n a_n m^{n-1} = 0 \tag{A4}$$

Further, the coefficients in the curve control equation should be expressed in terms of geometric quantities such as the nose radius, tail radius, and volume. The corresponding linear system is then established. In general, the radius of curvature R of the curve can be written as

$$R = \pm \frac{1}{\frac{d^2X}{dY^2}} \left[1 + \left(\frac{dX}{dY} \right)^2 \right]^{3/2} \tag{A5}$$

This equation can be nondimensionalized as

$$r = \pm \frac{1}{\frac{d^2x}{dy^2}} \left[1 + \frac{l^2}{d^2} \left(\frac{dx}{dy} \right)^2 \right]^{3/2} \tag{A6}$$

Taking successive derivatives of Equation (A1) with respect to y gives

$$2y = \left(a_1 + 2a_2 x + \ldots + n a_n^{n-1} \right) \frac{dx}{dy} \tag{A7}$$

$$2 = \left(a_1 + 2a_2 x + \ldots + n a_n^{n-1} \right) \frac{d^2x}{dy^2} + \left[2a_2 + \ldots + n(n-1) a_n^{n-2} \right] \left(\frac{dx}{dy} \right)^2 \tag{A8}$$

In Equation (A7), if $a_1 \neq 0$, then $x = 0$ and $\frac{dx}{dy} = 0$. Substituting these conditions into Equation (A8) gives $\frac{d^2x}{dy^2} = \frac{2}{a_1}$. Further substituting this result into Equation (A6) gives the relationship between the curve control equation and the nose radius of curvature:

$$a_1 = 2r_o \tag{A9}$$

If $a_1 = 0$, then $r_o = 0$, which means that the nose of the envelope is sharp and corresponds to $x = 0$.

Similarly, when $x = 1$, y $= 0$, from Equation (A7), it can be seen that $\frac{dx}{dy} = 0$. Therefore

$$a_1 + 2a_2 + 3a_3 + \ldots + n a_n = 0 \tag{A10}$$

Combining Equations (A6) and (A8) gives the relationship between the curve control equation and the tail radius of curvature:

$$a_1 + 2a_2 + 3a_3 + \ldots + n a_n = -2r_1 \tag{A11}$$

At $x = 1$, $r_1 = 0$, which means that the tail is sharp.

The volume V of the airship envelope can be expressed as

$$V = \int_0^l \pi Y^2 dX = \pi d^2 l \int_0^1 y^2 dx \tag{A12}$$

Substituting y^2 in Equation (A1) gives the relationship between the curve control equation and the prismatic coefficient:

$$\frac{1}{2}a_1 + \frac{1}{3}a_2 + \frac{1}{4}a_3 + \ldots + \frac{1}{n+1}a_n = \frac{1}{4}C_p \tag{A13}$$

In summary, all the constraints for the sixth-order polynomial can be written as follows:

$$y^2(0) = 0 \tag{A14}$$

$$y^2(1) \Rightarrow a_1 + 2a_2 + 3a_3 + \ldots + na_n = 0 \tag{A15}$$

$$\left.\frac{dy}{dx}\right|_0 \Rightarrow a_1 = 2r_o \tag{A16}$$

$$\left.\frac{dy}{dx}\right|_1 \Rightarrow a_1 + 2a_2 + 2a_3 + \ldots + na_n = -2r_1 \tag{A17}$$

$$y^2(m) \Rightarrow a_1 m + a_2 m^2 + a_3 m^3 + \ldots + a_n m^n = \frac{1}{4} \tag{A18}$$

$$\frac{dy}{dx}|_m \Rightarrow a_1 + 2a_2 m + 3a_3 m^2 + \ldots + na_n m^{n-1} = 0 \tag{A19}$$

$$\int_0^1 y^2(x)dx \Rightarrow \frac{1}{2}a_1 + \frac{1}{3}a_2 + \frac{1}{4}a_3 + \ldots + \frac{1}{n+1}a_n = \frac{1}{4}C_p \tag{A20}$$

A linear system is then established and rewritten in matrix form:

$$AX = B \tag{A21}$$

$$\begin{bmatrix} 1 & 1 & 1 & 1 & 1 & 1 \\ 1 & 0 & 0 & 0 & 0 & 0 \\ 1 & 2 & 3 & 4 & 5 & 6 \\ m & m^2 & m^3 & m^4 & m^5 & m^6 \\ 1 & 2m & 3m^2 & 4m^3 & 5m^4 & 6m^5 \\ \frac{1}{2} & \frac{1}{3} & \frac{1}{4} & \frac{1}{5} & \frac{1}{6} & \frac{1}{7} \end{bmatrix} \begin{bmatrix} a_1 \\ a_2 \\ a_3 \\ a_4 \\ a_5 \\ a_6 \end{bmatrix} = \begin{bmatrix} 0 \\ 2r_o \\ -2r_1 \\ \frac{1}{4} \\ 0 \\ \frac{1}{4}C_p \end{bmatrix} \tag{A22}$$

References

1. Liao, L.; Pasternak, I. A review of airship structural research and development. *Prog. Aerosp. Sci.* **2009**, *45*, 83–96. [CrossRef]
2. Yang, X.X.; Liu, D.N. Conceptual design of stratospheric airships focusing on energy balance. *J. Aerosp. Eng.* **2018**, *31*, 04017094. [CrossRef]
3. Jing, Y.H.; Wu, Y.; Tang, J.W.; Zhou, P.; Duan, D. Receding horizon trajectory generation of stratospheric airship in low-altitude return phase. *Aerospace* **2022**, *9*, 670. [CrossRef]
4. Liang, R.W.; Hassanalian, M. Adaptive neural network tracking control for stratospheric airships with enhanced monotone tube prescribed performance. *Aerosp. Sci. Technol.* **2026**, *177*, 112801. [CrossRef]
5. Bu, S.F.; Xie, W.M.; Peng, X.D.; Shen, X.; Ren, J.; Qin, R. A spatio-temporal foresight reinforcement-learning framework for long-term station-keeping of stratospheric airships. *Aerospace* **2026**, *13*, 551. [CrossRef]
6. Qi, L.L.; Yang, X.X.; Deng, X.L.; Bai, F.; Ma, Z. Stratospheric airship flight trajectory envelope prediction based on wind field uncertainty model. *Chin. J. Aeronaut.* **2026**, *39*, 103956. [CrossRef]
7. Yang, Y.N.; Wu, J.; Zheng, W. Design, modeling and control for a stratospheric telecommunication platform. *Acta Astronaut.* **2012**, *80*, 181–189. [CrossRef]
8. Roney, J.A.; Mourning, R.L. Balloon-borne planetary atmospheric sounder tested in the terrestrial environment. *Acta Astronaut.* **2007**, *60*, 96–110. [CrossRef]
9. Li, Y.K.; Liang, H.Q.; Wang, Y.; Liu, D. Nonlinear response prediction of stratospheric airship envelope differential pressure via multimodal coupling and multiscale decomposition. *Aerosp. Sci. Technol.* **2026**, *178*, 112380. [CrossRef]
10. Li, Z.B.; Yang, Y.C.; Cai, R.; Li, T. Biaxial constitutive relation and strength criterion of envelope materials for stratospheric airships. *Aerospace* **2026**, *13*, 147. [CrossRef]

11. Meng, J.H.; Liu, S.Y.; Yao, Z.B.; Lv, M. Optimization design of a thermal protection structure for the solar array of stratospheric airships. *Renew. Energy* **2019**, *133*, 593–605. [CrossRef]
12. Du, H.; Lyu, M.; Yu, C.; Wu, Y.; Wu, Y.; Sun, K. Numerical simulation of fluid–thermal–structural coupling characteristics of stratospheric non-rigid airship. *Chin. J. Aeronaut.* **2024**, *37*, 224–236. [CrossRef]
13. Zou, T.; Sun, K.W.; Liang, H.Q.; Lou, W.; Yuan, J. Application advantages of bifacial photovoltaic array on stratospheric airship based on power-to-areal-density ratio. *IEEE Trans. Aerosp. Electron. Syst.* **2025**, *61*, 16121–16132. [CrossRef]
14. Cheng, J.S.; Bin, D.J.; Gong, X.R.; Wang, S.; Jiang, B.Y.; Nie, Y. Dynamic characteristics of flexible hull–propulsion systems in stratospheric airships: FEA and experimental study. *Aerosp. Sci. Technol.* **2025**, *165*, 110529. [CrossRef]
15. Manikandan, M.; Pant, R.S. A comparative study of conventional and tri-lobed stratospheric airships. *Aeronaut. J.* **2021**, *125*, 1434–1466. [CrossRef]
16. Colozza, A.J.; Dolce, J.L. *Initial Feasibility Assessment of a High Altitude Long Endurance Airship*; NASA/CR–2003-212724; NASA Glenn Research Center: Cleveland, OH, USA, 2003.
17. Alam, M.I.; Pasha, A.A.; Jameel, A.G.A.; Ahmed, U. High altitude airship: A review of thermal analyses and design approaches. *Arch. Comput. Methods Eng.* **2023**, *30*, 2289–2339. [CrossRef]
18. Hu, K.; Zhou, J.; Zhang, X. A stratospheric wind field interpolation method based on geostrophic wind model. *J. Beijing Univ. Aeronaut. Astronaut.* **2022**, *48*, 639–646.
19. Wang, Q.B.; Chen, J.A.; Fu, G.Y.; Duan, D.-P. An approach for shape optimization of stratosphere airships based on multidisciplinary design optimization. *J. Zhejiang Univ. Sci. A* **2009**, *10*, 1609–1616. [CrossRef]
20. Liang, H.Q.; Zhu, M.; Guo, X.; Zheng, Z. Conceptual design optimization of high altitude airship in concurrent subspace optimization. In Proceedings of the 50th AIAA Aerospace Sciences Meeting, Nashville, TN, USA, 9–12 January 2012; AIAA 2012-1180.
21. Hoerner, S.F. *Fluid-Dynamic Drag: Practical Information on Aerodynamic Drag and Hydrodynamic Resistance*; Hoerner Fluid Dynamics: Brick Town, NJ, USA, 1965.
22. Tatsios, G.; Chinnappan, A.K.; Kamal, A.; Vasileiadis, N.; Docherty, S.Y.; White, C.; Gibelli, L.; Borg, M.K.; Kermode, J.R.; Lockerby, D.A. A DSMC–CFD coupling method using surrogate modelling for low-speed rarefied gas flows. *J. Comput. Phys.* **2025**, *520*, 113500. [CrossRef]
23. Shi, Y.Y.; Tang, X.; Wu, P.F.; Yang, T.; Feng, K.; Wang, B. Global sensitivity analysis of supersonic laminar wing transition considering multi-source random uncertainties. *Aerosp. Sci. Technol.* **2026**, *173*, 111765. [CrossRef]
24. Esfahanian, V.; Izadi, M.J.; Bashi, H.; Ansari, M.; Tavakoli, A.; Kordi, M. Aerodynamic shape optimization of gas turbines: A deep learning surrogate model approach. *Struct. Multidiscip. Optim.* **2024**, *67*, 2. [CrossRef]
25. Nikas, I.A.; Georgopoulos, V.P.; Loukopoulos, V.C. Selective multistart optimization based on adaptive Latin hypercube sampling and interval enclosures. *Mathematics* **2025**, *13*, 1733. [CrossRef]
26. Gao, S.Z.; Zhao, Y.K.; Zhao, X.D.; Zhang, Y. Application of response surface method based on new strategy in structural reliability analysis. *Structures* **2023**, *57*, 105202. [CrossRef]
27. Sacks, J.; Welch, W.J.; Mitchell, T.J.; Wynn, H.P. Design and analysis of computer experiments. *Stat. Sci.* **1989**, *4*, 409–435. [CrossRef]
28. Hardy, R.L. Multiquadric equations of topography and other irregular surfaces. *J. Geophys. Res.* **1971**, *76*, 1905–1915. [CrossRef]
29. Zhang, Y.; Wang, X.L. Global sensitivity and design space of drag characteristics of parametric airship hull. *J. Harbin Inst. Technol.* **2021**, *53*, 54–61. [CrossRef]
30. Lv, M.Y.; Yao, Z.B.; Zhang, L.C.; Du, H.F.; Meng, J.H.; Li, J. Effects of solar array on the thermal performance of stratospheric airship. *Appl. Therm. Eng.* **2017**, *124*, 22–33. [CrossRef]
31. Dorrington, G.E. Drag of spheroid-cone shaped airship. *J. Aircr.* **2006**, *43*, 363–371. [CrossRef]
32. Alam, M.I.; Pant, R.S. Multi-objective multidisciplinary design analyses and optimization of high altitude airships. *Aerosp. Sci. Technol.* **2018**, *78*, 248–259. [CrossRef]
33. Katoch, S.; Chauhan, S.S.; Kumar, V. A review on genetic algorithm: Past, present, and future. *Multimed. Tools Appl.* **2021**, *80*, 8091–8126. [CrossRef] [PubMed]
34. Goldberg, D.E. *Genetic Algorithms in Search, Optimization, and Machine Learning*; Addison-Wesley: Reading, MA, USA, 1989.
35. Yang, Y.C.; Wang, S.; Gu, Y.D.; Li, Y.T.; Miao, J.G. Shape optimization design and simulation of near-space airship. *Chin. Space Sci. Technol.* **2011**, *31*, 76–83.
36. Alam, M.I.; Pant, R.S. Multidisciplinary approach for solar area optimization of high altitude airships. *Energy Convers. Manag.* **2018**, *164*, 301–310. [CrossRef]

Disclaimer/Publisher's Note: The statements, opinions and data contained in all publications are solely those of the individual author(s) and contributor(s) and not of MDPI and/or the editor(s). MDPI and/or the editor(s) disclaim responsibility for any injury to people or property resulting from any ideas, methods, instructions or products referred to in the content.